Anti-reflection subwavelength gratings for InP-based waveguide facets

Please check the document version of this publication:

• A submitted manuscript is the version of the article upon submission and before peer-review. There can be important differences between the submitted version and the official published version of record. People interested in the research are advised to contact the author for the final version of the publication, or visit the DOI to the publisher's website.
• The final author version and the galley proof are versions of the publication after peer review.
• The final published version features the final layout of the paper including the volume, issue and page numbers.

Link to publication

Optics Letters

Anti-reflection subwavelength gratings for InP-based waveguide facets

Lukas Puts,[1,*] **Xaveer Leijtens,**[1] **Pavel Cheben,**[2] **Jens Schmid,**[2] **Sander Reniers,**[1] **and Daniele Melati**[3]

[1]*Photonic Integration Group, Department of Electrical Engineering, Eindhoven University of Technology, P.O. Box 513, Eindhoven 5600MB, The Netherlands*
[2]*National Research Council Canada, Ottawa, Ontario K1A 0R6, Canada*
[3]*Centre for Nanoscience and Nanotechnologies, CNRS, Université Paris-Saclay, 10 Bv. Thomas Gobert, 91120 Palaiseau, France*
Corresponding author: l.puts@tue.nl

We demonstrate the anti-reflection properties of lithographically defined subwavelength gratings applied to the facets of integrated waveguides realized in the InP membrane-on-silicon platform. The subwavelength gratings are based on the gradient index effect to create a smooth index transition between the core material and air, making it possible to obtain reflections below −30 dB at a wavelength of 1550 nm for both TE and TM polarized modes, as shown by 3D finite-difference time-domain simulations. Characterizations performed using Mach–Zehnder interferometers as test structures show relative reflections as low as −25 dB, confirming the effectiveness of the technique.   © 2021 Optical Society of America

Controlling reflections at waveguide facets is crucial for optimal performance of photonic integrated devices and circuits. A notable example is the strong effect that small reflections can have on the dynamics of integrated lasers [1,2]. For fiber-to-chip edge couplers, low reflections are needed to achieve high coupling efficiency. Waveguide facets represent one of the main sources of reflections, generated by abrupt index transitions between the waveguide materials and air. For typical single-mode waveguides in silicon and III-V semiconductor platforms, cleaved facets without adaptation structures have a strong reflectivity of about 30% [3]. Commonly, single or multilayer anti-reflection (AR) thin films with a precisely engineered thickness and refractive index are used to reduce these reflections. When exploited on InP waveguide facets, this approach allows to reduce reflections of the order of −30 dB [4]. For specific materials such as aluminum-containing alloys, thin films also provide a passivation function, minimizing the interaction between the semiconductor material and oxygen. This is an important aspect that affects the properties of active material. However, thin films have some important drawbacks. Complex vacuum deposition techniques are required to apply films on a cleaved facet, which can be done only as a post-processing step, increasing fabrication complexity. Furthermore, the films may become mechanically unstable under thermal cycling, resulting in loss of performance [5]. Another approach that is often

applied is the use of angled facets. By changing the facet angle, reflectivity reduction of about −40 dB for the fundamental mode has been demonstrated in III-V waveguides [6]. However, by increasing the facet angle, higher order mode reflections can be generated. This can be especially problematic in wide waveguides supporting higher order modes [7].

Another strategy to minimize reflections is the patterning of the waveguide facet with a subwavelength grating (SWG). This type of structure has been used in a wide range of applications to control reflections. For example, SWGs have been applied on bulk surfaces such as solar cells to optimize performance [8]. The same concept has been exploited to reduce reflections from the facets of quantum cascade lasers by patterning a rectangular grating using focused ion beam (FIB) milling after chip fabrication. Reflections as low as 1%–3% have been achieved using this method [9]. However, FIB milling can be applied only during post-processing after each individual chip has been diced and facets have been formed, largely complicating fabrication. Moreover, ion sputtering and a diverging ion beam resulted in significant differences between the designed and fabricated grating geometry, indicating FIB might not be ideal to fabricate SWGs. The use of lithographically defined SWGs as anti-reflective coatings, first demonstrated by Schmid *et al.* [5], eliminates the need for chip-level post-processing. A grating with triangular teeth was fabricated using electron beam lithography (EBL) on a silicon-on-insulator (SOI) platform. Reflections as low as 2% and 2.4% for the fundamental TE and TM polarized modes were achieved, respectively [10]. Moreover, triangular teeth result in a grating that acts as an AR layer with a graded instead of uniform index, reducing its wavelength sensitivity. While extensively studied for SOI waveguides [11–14], few investigations have been reported so far on the use of SWGs on InP-based platforms. The possibility to control reflections by subwavelength patterned geometries is of particular interest because of the wide range of active components available on III-V platforms, which often heavily rely on thin-film AR facet coatings.

In this Letter, we simulate, design, and experimentally demonstrate an AR subwavelength waveguide facet grating on the InP-membrane-on-silicon (IMOS) platform [15].

The IMOS platform comprises a 300 nm thick InP photonic membrane on a standard silicon wafer. On top of this passive waveguiding layer, an active layer consisting of InGaAsP multiple quantum well for active devices can be incorporated. The passive layer stack for a standard 400 nm wide single-mode IMOS waveguide is shown in Fig. 1(a). First, the InP waveguide pattern is transferred to a small InP wafer using EBL. The wafer is then flipped and bonded to a silicon wafer using the adhesive polymer divinylsiloxane-bis-benzocyclobutene (DVS-BCB) and a 200 nm thick SiO_2 bonding layer. The InP substrate and InGaAs etch-stop layers are removed by selective wet-chemical etching. The thin patterned InP membrane remains on the silicon wafer [15]. Due to the large index differences among InP ($n = 3.17$), BCB ($n = 1.54$), and SiO_2 ($n = 1.45$), very compact waveguides can be realized. The resulting electric field distribution for the fundamental TE and TM modes is shown in Figs. 1(c) and 1(d). Most of the electric field of the fundamental TE mode is concentrated in the waveguide core, whereas the TM mode is primarily localized in the oxide cladding below and air above the core. To realize the AR structure, the waveguide core is patterned with a gradient index (GRIN) SWG consisting of an array of triangles, as depicted in Fig. 1(b). When the period of the grating is smaller than the wavelength in the medium, the structure can be approximated as an equivalent material with a refractive index gradually changing from that of the waveguide core to the index of the cladding [16]. The gradual transition from core to cladding suppresses facet reflections by eliminating the abrupt termination of the waveguide. Since index grading does not rely on interference effects, it is inherently less wavelength sensitive compared to common thin-film AR layers [5].

A combination of 3D finite-difference time-domain (FDTD) simulations for accurate reflection evaluation and 2D FDTD for tolerance analysis was used to design the AR structures. For 2D simulations, a commercial implementation of the effective index method was exploited to account for the non-uniform vertical layer stack and compute the equivalent refractive indices of the complex waveguide structure. For both types of simulations, the facet model comprises a waveguide and a triangular grating with a fixed subwavelength period of 400 nm, as shown in Fig. 1(b). The grating length is varied from 0 to 2 μm, and the waveguide width is varied from 2 to 4 μm. The fundamental TE or TM mod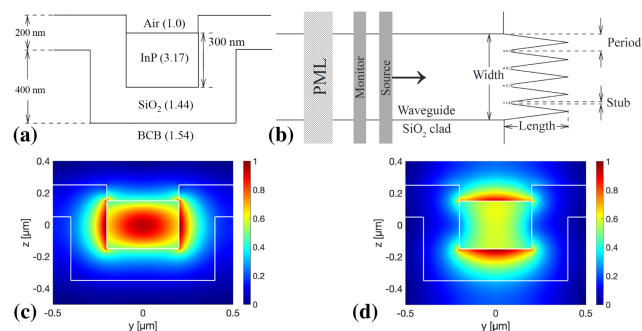e is injected from the left at $\lambda_0 = 1550$ nm towards the grating. A power monitor left of the source measures the amount of light reflected from the SWG structure.

The TE and TM reflections calculated by 3D FDTD as a function of the grating teeth length are shown in Figs. 2 and 3, respectively. For clarity, the simulation results for a 2 μm wide SWG are marked with blue dots, and unmarked curves show the results for a 4 μm wide SWG. The dashed-dotted lines show the total reflections (TE), and solid lines show the modal reflections (TE_0). The latter refers to the amount of reflected power coupled into the counterpropagating fundamental mode. At a grating teeth length of 0 nm, the structure is simply a flat facet with a reflection of ∼25%, as expected (Fig. 2). From these simulations, it is clear that the facet reflection decreases rapidly with increasing grating teeth length. The TE_0 reflection drops to about −30 dB for a grating teeth length of approximately 0.5 μm. The difference between the modal and total reflection simulations is small, indicating that mode conversion is small. The oscillatory behavior of the reflection results in three other minima at 1 μm, 1.4 μm, and 1.85 μm. Simulated reflections for these minima are between −30 and −35 dB. The width of the waveguide has only a small influence on the reflection.

From these simulations, it follows that the preferred design spot for a substantial reduction in TE reflection is the first minimum, at about 0.51 μm. This results in a compact device with the smallest possible aspect ratio. Even lower reflection could be achieved for longer grating teeth lengths; that, however, would require structures with larger aspect ratios, making fabrication more challenging.

The results for TM simulations are shown in Fig. 3. The simulated structures are the same as described in the previous paragraph. Without any grating teeth (length of 0 nm), the
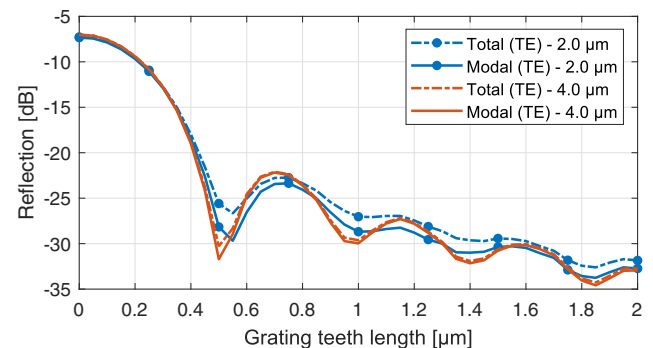
Fig. 2. 3D FDTD simulation results for the reflection of the TE polarized mode as a function of the grating teeth length.

Fig. 1. (a) Schematic cross section of a standard IMOS waveguide, indicating the materials with respective refractive indices and dimensions. (b) Top view of the SWG patterned on the waveguide facet and FDTD simulation layout. (c), (d) Fundamental TE and TM electric field profiles in a 400 nm wide IMOS waveguide, respectively.
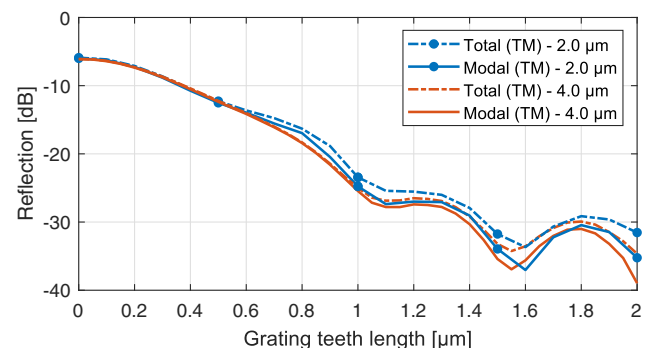

Fig. 3. 3D FDTD simulation of the reflection of the TM polarized mode as a function of the grating teeth length.

reflections are 30%, which decrease to values below -30 dB for grating teeth length larger than 1.4 µm. The SWG teeth are parallel to the oscillations of the electric field for TM polarization, and as a result, the AR effect is less strong compared to TE polarization. This was previously observed in AR SWGs on SOI waveguides [5]. The preferred design spot in this case is 1.55 µm, at which a reflection of about -35 dB is achieved.

As discussed above, the optimal design points have been chosen to obtain the shortest possible grating teeth. This resulted in different optimum lengths for TE and TM modes and hence a dependence of performance on polarization. It should be noted, however, that different choices are also possible. For circuits requiring low facet reflections for both polarizations simultaneously, a teeth length of 1.µm would reduce reflection below -20 dB for both TE and TM modes at the expense of a more challenging fabrication. Similarly, designs with reflections below -30 dB independent of polarization can be found.

Next, fabrication tolerances of the proposed designs are investigated. Due to the diffraction limit and electron backscattering in the photoresist, the resolution for EBL is limited to approximately 20 nm. There are two regions where the SWG feature size is below 20 nm and are hence difficult to define using EBL. The tip of each tooth will result in a rounded shape with a certain radius, and the region between the bases of two adjacent teeth will not be defined accurately. Additionally, for SWGs with high aspect ratios, latter regions can be also difficult to etch due to the etch lag effect [17]. To ensure reliable fabrication, a "stub" is placed between the bases of adjacent teeth, as shown in Fig. 1(b). The size of this stub is made equal to the resolution of the EBL, decreasing the etch lag effect in this particular region. 2D FDTD simulations show that a stub of 20 nm adds approximately 3.2 and 2.1 dB to the total and modal TE reflections, respectively. Random and systematic process-induced fluctuations such as variations in focus, dose, and resist quality influence critical dimensions (CDs). These fluctuations may result in uniform CD variations of several nanometers with respect to the nominal design. 2D FDTD simulations for the grating with a waveguide width of 4 µm, length of 0.51 µm, and stub of 20 nm were carried out to investigate the effect of uniform CD variation. Changing all structure dimensions by 10 nm resulted in an increase in facet reflection of approximately 3 dB.

To experimentally characterize reflections induced by the facet grating, we designed the unbalanced Mach–Zehnder interferometer (MZI) schematically shown in Fig. 4. The MZI is based on three 2×2 multimode interference (MMI) couplers, leveraging their low backscattering characteristics [18] and nominal waveguides with a width of 400 nm. One of the arms contains an MMI coupler and two 62 µm long linear adiabatic tapers terminated with two identical SWG gratings R_1 and R_2. The phase shift $\Delta\varphi$ in this arm is the result of the extra optical path length of approximately 1135 µm. Surface grating couplers are used to couple light into and out of the circuit (P_{in}, P_2, P_3, P_4).

To use this structure to measure the SWG reflectivity, the output power of the bar (P_3) and cross (P_4) ports as a function of the wavelength can be derived using the expression for the transfer function of a single MZI [19]. The contrast ratio C, defined as the ratio between the minima and maxima of the fringes in the MZI transmission spectrum for either of the two output ports P_3 and P_4, can be calculated as follows:
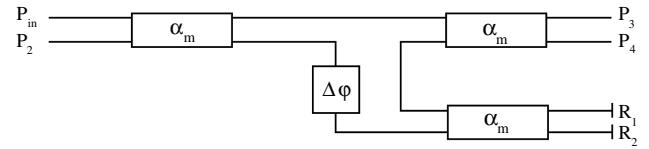
Fig. 4. Block diagram of the unbalanced MZI used for AR SWG characterization. Input and outputs ports $P_{\mathrm{in}} - P_4$ and the SWGs under test R_1, R_2 are marked.

$$C = \frac{P_{\mathrm{out,max}}}{P_{\mathrm{out,min}}} = \frac{\left(\left(\sqrt{R_1} + \sqrt{R_2}\right)\alpha_{\mathrm{m}}e^{-\alpha l} + 2\right)^2}{\left(\left(\sqrt{R_1} + \sqrt{R_2}\right)\alpha_{\mathrm{m}}e^{-\alpha l} - 2\right)^2}, \quad \text{(1)}$$

where R_1 and R_2 are the corresponding SWG reflectivities, α_{m} the MMI coupler loss, α the waveguide propagation loss, and l the MZI arm length difference. Assuming $R_1 = R_2 = R$, the reflectivity R can hence be determined from the measured contrast ratio. A total of 20 MZIs with 4 µm wide SWGs and grating teeth length ranging from 0 to 1.7 µm were designed on a 4×6 mm^2 IMOS cell. The grating period was fixed at 400 nm. Two identical cells were patterned by EBL, and proximity effect correction (PEC) and shape correction were applied to the graphic data system file to compensate for electron back scattering and optimize the dose locally.

TE polarized light was coupled in and out of the circuit using surface grating couplers optimized for TE coupling (Fig. 5). Due to variations in fabrication, the optimal coupling efficiency of the surface grating couplers was shifted to 1535 nm from the designed 1550 nm. The influence of this shift on the performance of the designed grating was evaluated using 2D FDTD simulations, and a negligible difference of less than 0.25 dB was found, confirming the broadband performance of the proposed device. The wavelength of the input light was swept from 1465 to 1575 nm using a tunable laser source. The chip temperature was maintained at 21°C using a Peltier element mounted on a copper chuck. The output light intensity was measured by a power meter.

Two examples of the measured spectra at the output port P_3 for the test MZI with SWG teeth lengths of 0.2 and 0.5 µm are shown in Fig. 6. The latter is the preferred design spot for the TE polarized mode and, as expected, its AR properties translate into a reduced contrast ratio of the spectral fringes compared to the SWG with a grating teeth length of 0.2 µm.

The mean and standard deviation of the contrast ratio C for each of the 20 MZIs of one design cell was determined from multiple fringes in the spectral range from 1520 to 1540 nm of the individual devices. The calculated relative reflections derived from (1) are then normalized using the 3D FDTD simulations of the SWG with a grating teeth length of 0.2 µm. The solid line in Fig. 7 shows the results of this analysis as a function of the
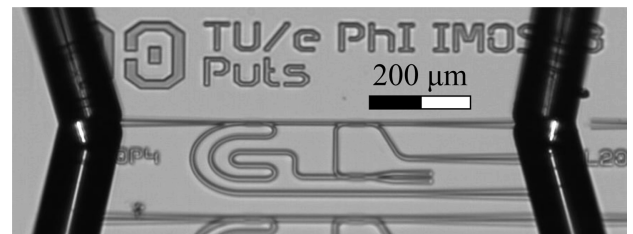
Fig. 5. Photograph of part of the IMOS chip showing one Mach–Zehnder interferometer and the input and output fibers at an angle of 10° for optimal coupling.
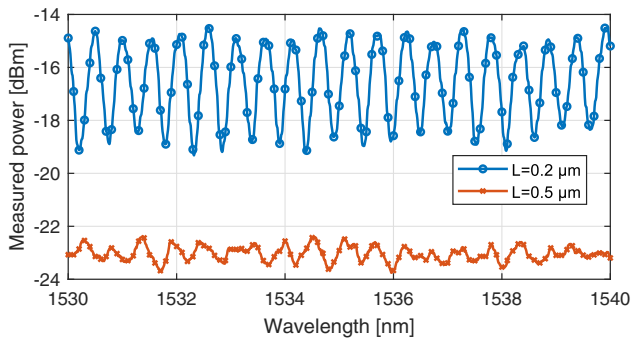
Fig. 6. Output power at P_3 of two MZIs with facet grating lengths of 0.2 and 0.5 μm. Lower fringe contrast of the SWG with longer grating teeth length is due to the AR properties. Contrast ratios for these test structures are 2.484 ± 0.332 and 1.176 ± 0.0815 for lengths of 0.2 and 0.5 μm, respectively. To prevent cluttering of data points, only a quarter of the measurements is marked.
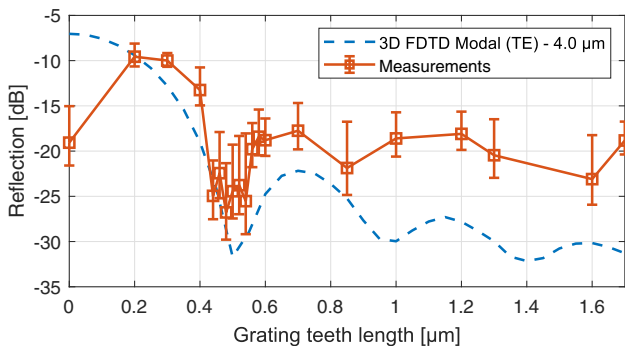

Fig. 7. Overlay of 3D FDTD simulations and experimental results in the IMOS platform. The error bars show the standard deviation in the measurement.

grating teeth length. Squares mark the mean relative reflections and the error bars the standard deviations. The dashed line shows the modal TE 3D FDTD simulation results for reference (same data as in Fig. 2). Results of the simulations and measurements are in good agreement and show a similar trend of reflection as a function of grating teeth length. The reflections drop rapidly with increasing grating teeth length, and similar to the simulations, the first minimum is located approximately at 0.5 μm at a value of −18 dB below the expected flat facet reflection of −6.8 dB. Relative reflectivity between 0.6 and 1.7 μm is substantially higher compared to the simulations. This is likely related to the challenges in etching SWGs with large aspect ratios. Moreover, the measured reflection of a flat facet is substantially lower than what is expected from simulations. However, this data point is likely an outlier caused by the test device since reflections of about −7 dB were measured for flat waveguide facets on dedicated test structures, in line with 3D FDTD predictions.

In conclusion, we have designed and experimentally demonstrated an effective AR strategy for InP IMOS waveguides by exploiting SWGs. These lithographically defined structures are particularly interesting for InP-based technology platforms since the performance of active components often relies heavily on AR coatings deposited during post-processing. Simulated TE_0 mode reflections are as low as −30 dB for an SWG with a grating teeth length of 0.51 μm, width of 4 μm, and fixed period of 400 nm. This results in a compact design with a relatively low aspect ratio, which is beneficial for fabrication. Reflections as low as −35 dB are achieved for the TM_0 mode for SWGs with a grating teeth length of 1.55 μm. The AR effect was experimentally demonstrated using MZIs as test structures, achieving a reflection minimum of −25 dB for the TE polarized mode for the optimal SWG design parameters predicted by 3D FDTD. The possibility to reliably realize gratings with teeth longer than 1 μm could provide even better suppression of facet reflectivity for the TE mode, access to an effective anti-reflective device for the TM mode, as well as polarization insensitive designs.

Disclosures. The authors declare no conflicts of interest.

Data Availability. Data underlying the results presented in this paper are not publicly available at this time but may be obtained from the authors upon reasonable request.

REFERENCES

1. P. Zorabedian, IEEE J. Quantum Electron. **30**, 1542 (1994).
2. K. Petermann, IEEE J. Sel. Top. Quantum Electron. **1**, 480 (1995).
3. D. Melati, F. Morichetti, and A. Melloni, Opt. Quantum Electron. **45**, 309 (2013).
4. M. Sun, S. Tan, F. Guo, S. Liu, Q. Kan, D. Lu, R. Zhang, W. Zhao, S. Liang, W. Wang, R. Broeke, F. M. Soares, and C. Ji, IEEE Photon. J. **8**, 1502508 (2016).
5. J. Schmid, P. Cheben, S. Janz, J. Lapointe, A. Delâge, A. Densmore, B. Lamontagne, P. Waldron, and D. Xu, Proc. SPIE **6796**, 67963E (2007).
6. Y. Matsuoka, S. Mathonnière, M. P. Semtsiv, and W. T. Masselink, Proc. SPIE **10553**, 105531L (2018).
7. P. Zorabedian, *Tunable External-Cavity Semiconductor Lasers* (Academic, 1995), Optics and Photonics, pp. 349–442.
8. N. Das and S. I. Sen, in *22nd Australasian Universities Power Engineering Conference (AUPEC)* (2012), pp. 1–5.
9. A. O. Dirisu, G. Silva, Z. Liu, C. F. Gmachl, F. J. Towner, J. Bruno, and D. L. Sivco, IEEE Photon. Technol. Lett. **19**, 221 (2007).
10. J. Schmid, P. Cheben, S. Janz, J. Lapointe, E. Post, and D.-X. Xu, Opt. Lett. **32**, 1794 (2007).
11. P. Cheben, R. Halir, J. Schmid, H. Atwater, and D. Smith, Nature **560**, 565 (2018).
12. R. Halir, A. Ortega-Moñux, D. Benedikovic, G. Z. Mashanovich, J. G. Wangüemert-Pérez, J. H. Schmid, I. Molina-Fernández, and P. Cheben, Proc. IEEE **106**, 2144 (2018).
13. R. Halir, P. J. Bock, P. Cheben, A. Ortega-Moñux, C. Alonso-Ramos, J. H. Schmid, J. Lapointe, D.-X. Xu, J. G. Wangñemert-Pérez, I. Molina-Fernández, and S. Janz, Laser Photon. Rev. **9**, 25 (2015).
14. J. Schmid, P. Cheben, S. Janz, J. Lapointe, E. Post, A. Delâge, A. Densmore, B. Lamontagne, P. Waldron, and D.-X. Xu, Adv. Opt. Technol. **2008**, 685489 (2008).
15. J. J. G. M. van der Tol, Y. Jiao, J. P. Van Engelen, V. Pogoretskiy, A. A. Kashi, and K. Williams, IEEE J. Quantum Electron. **56**, 6300107 (2020).
16. S. M. Rytov, Sov. Phys. JETP **2**, 466 (1956).
17. J. Bolk, "ArF scanner lithography for InP photonic integrated circuit fabrication," Ph.D. thesis (Eindhoven University of Technology, 2020).
18. E. Kleijn, M. K. Smit, and X. J. M. Leijtens, Proc. SPIE **8781**, 878104 (2013).
19. C. K. Madsen and J. H. Zhao, *Digital Filter Concepts for Optical Filters* (Wiley, 2001), Chap. 3, pp. 95–164.